Tracking the Redox Reaction Induced Reconstruction of NiAu Nanoparticles via Environmental Scanning Transmission Electron Microscopy

Ming Hao[a,b,‡], Hao Li[c,‡], Wei Liu[d,*], Tianyi Ma[e], Jinsheng Liang[a,b], Kai Sun[f,*], Hiroaki Matsumoto[g], Fei Wang[a,b,*]

[a] *Key Laboratory of Special Functional Materials for Ecological Environment and Information (Hebei University of Technology), Ministry of Education, Tianjin 300130, China.*

[b] *Institute of Power Source and Ecomaterials Science, Hebei University of Technology, Tianjin 300130, China.*

[c] *Department of Physics, Technical University of Denmark, Kongens Lyngby2800, Denmark.*

[d] *Dalian National Laboratory for Clean Energy, Dalian Institute of Chemical Physics, Chinese Academy of Sciences, Dalian 116023, China.*

[e] *Centre for Translational Atomaterials, School of Science, Swinburne University of Technology, Hawthorn, VIC 3122, Australia.*

[f] *Department of Materials Science and Engineering, University of Michigan, Ann Arbor, MI 48109-2136, USA.*

[g] *Hitachi High-Technologies (Shanghai) Co., Ltd, Shanghai201203, China.*

‡ These authors contributed equally.

Experimental Sections

Synthesis of NiAu dumbbell. The synthesis procedure was similar as our former work[1] and all the reagents were in analytical grades and used without further purification. In brief, 0.2 mmol Ni(acac)$_3$ was dissolved in 10 mL oleylamine (OAm). The solution was heated up to 120 °C for 120 min under continuous magnetic stirring. Next, 100 mg trioctylphosphine oxide (TOPO) and 1 mL oleic acid (OA) were added into the solution under an Ar flux (purity > 99.999%) for additional 0.5 h and then the temperature was raised to 180 °C. Following, 2 mL toluene solution dissolved of 0.15 mmol H[AuCl$_4$]·4H$_2$O was poured into the Ni(acac)$_3$ solution rapidly and heated to 250 °C and maintained for 5 min. Finally, the original product was collected by centrifugation, washing and drying.

The oxidized and reduced sample for catalytic test was prepared through treating the fresh sample in a fixed-bed reactor under a controlled atmosphere and temperature.

Electron microscopy characterization. The ex situ TEM characterizations were all performed on a scanning transmission electron microscope (STEM, JEOL 3100R05 cold emission with a probe-aberration corrected). Both bright-field (BF) and dark-field (DF) signals were collected spontaneously to achieve comprehensive information of the same hybrid nanostructure. Specifically, the lens settings define the collect angle for HAADF imaging to be 59-200 mrad, which enables atomic-number contrast thus provides the direct observation on the distribution of Ni and Au atoms.

For IL-TEM experiments in this work, fresh sample was dispersed on a Mo grid and then imaged a specific place firstly. Following, the grid loaded with samples was fixed in a fixed-bed reactor with a controlled gas atmosphere and temperature-programmed system. After oxidative or reductive treatment (O_2 for oxidation and H_2 for reduction) in the reactor, the grid was transferred in air to the TEM, where IL-TEM images were acquired firstly.

In situ TEM experiments were performed on a cold-field emission HF5000 microscope (Hitachi High-Technologies Corporation, Japan) with a voltage of 200 kV and equipped with a Cs-corrector (0.078 nm of spatial resolution). The in situ TEM images were obtained under the HAADF mode at a collection angle range of 40-213 mrad when the gas was inlet and filled around the sample location. A specially designed gas nozzle was used to guide O_2 or H_2 gas into the microscope and control the internal pressure for the in situ oxidation and reduction reaction, respectively. The MEMS (microelectromechanical systems)-based heating holder (produced by Hitachi Company, Japan) with Ni-Au catalysts loaded on the Si_3N_4 membrane was adopted to start the following in situ reaction. A temperature ramping rate of 1 °C s^{-1} for the oxidation procedures at 300-400 °C (Supplementary Video 1 at a ×10 playback speed) and 0.5 °C s^{-1} for 400-500 °C (Supplementary Video 2 at a ×10 playback speed), and at a rate of 1 °C s^{-1} for the in situ reduction at 500-600 °C (Supplementary Video 3 at a ×10 playback speed). The post-analysis of these results was with the help of Digital Micrograph (GMS 3.22) as well as Image J (1.52a).

Catalytic property test. The 100 mg catalysts and 100 mg SiO_2 were tested in a single-pass, fixed-bed reactor which operated at atmospheric pressure with a GSV = 2 liters·min^{-1}·g·cat^{-1}. Reactant and product analysis were performed using a Thermo Fisher Antaris IGS FTIR Gas Analyzer. The reactor was operated with total gas flowrates in the range 200 mL·min^{-1}. The gas flow was consisted of 2000 ppm of NO and 2000 ppm of CO balanced with N_2. The temperature was measured by a K-type thermocouple within the quartz tube reactor, immediately upstream of the catalyst bed. The reactor heating rate was 2 °C/min.

Theoretical analysis. Spin-polarized density functional theory (DFT) calculations were conducted with the electronic exchange and correlations described by the generalized gradient approximation method and the functional developed by Perdew, Burke, and Ernzerhof.[2] The valence electrons were treated by expanding the Kohn-Sham wave functions in a plane-wave basis set.[3] The kinetic energy cutoff was set to 400 eV for all of the calculations. Convergence was defined after the all forces became lower than 0.05 eV/Å. The (3×3×1) *k*-point meshes were used to sample the Brillouin zone via the method developed by Monkhorst and Pack.[4] A four layer, (4×4), (111) surface was built for all of the calculations, with the bottom two layers constrained in bulk position. The structures were generated by our homemade Python scripts based on the Atomic Simulation Environment.[5] The selection of lattice constant was based on the Vegard's law described in Ref. 6. The binding energies of CO and NO were calculated by:

$$E_{CO/NO} = E_{tot} - E_{bare} - E_{CO/NO} \quad (1)$$

where E_{tot}, E_{bare}, and $E_{CO/NO}$ represent the total energies of the surface with adsorbate, the bare surface, and a CO or NO molecule in vacuum, respectively. The binding energies of O and H were calculated by:

$$E_{O/H} = E_{tot} - E_{bare} - \frac{1}{2}E_{O_2/H_2} \quad (2)$$

where E_{O_2/H_2} represents the total energy of an O_2/H_2 molecule in vacuum.

Table S1. Calculated binding energies and error bars on the Ni_3 site over the surfaces shown in Figure S13.

|	CO Binding	NO Binding	O Binding	H Binding
$Ni@Au_{0.25}Ni_{0.75}$	-1.75 eV	-2.31 eV	-2.02 eV	-0.48 eV
A	-1.79 eV	-2.35 eV	-2.04 eV	-0.50 eV
B	-1.81 eV	-2.39 eV	-2.08 eV	-0.51 eV
C	-1.82 eV	-2.42 eV	-2.10 eV	-0.52 eV
Average	-1.79 eV	-2.37 eV	-2.06 eV	-0.50 eV
Error bar	± 0.03 eV	± 0.05 eV	± 0.04 eV	± 0.02 eV
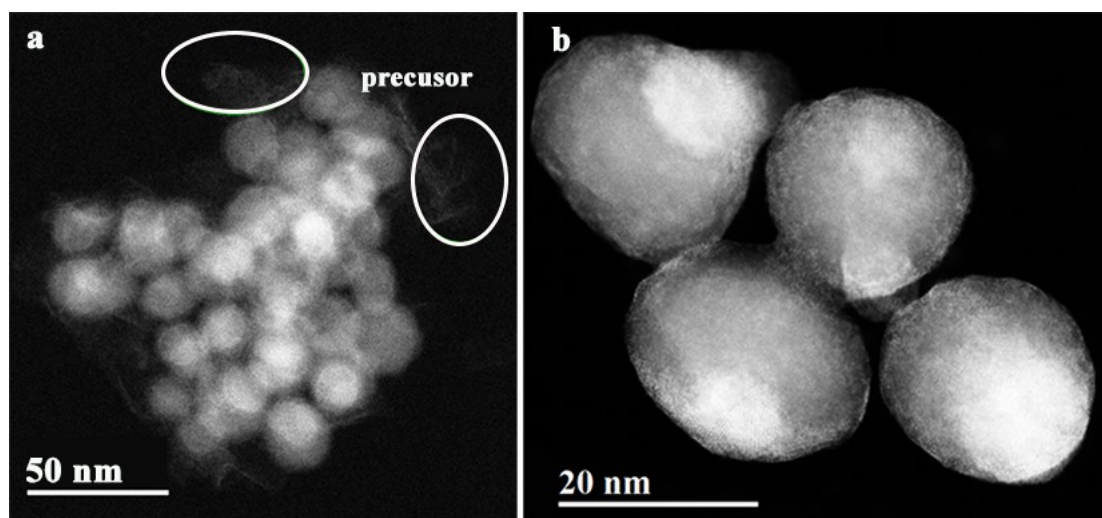
Figure S1. HAADF images of original NiAu NPs with residual Ni-OAm precursor covering on the surface (a) and NiAu NPs after annealing in vacuum at 300 °C for 15min (b).
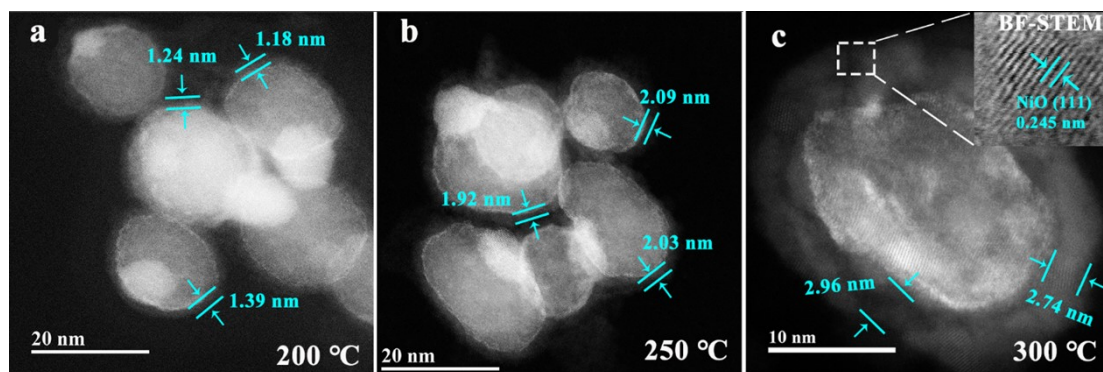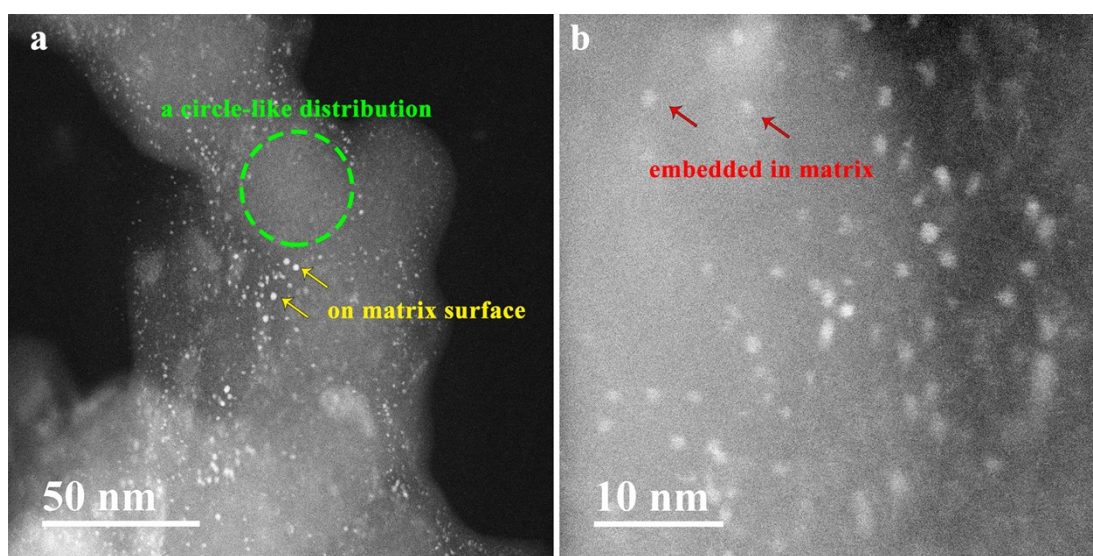
Figure S2. HAADF images of original NiAu after oxidation at 200 $^{\circ}$C (a), 250 $^{\circ}$C (b) and 300 $^{\circ}$C (c), respectively.
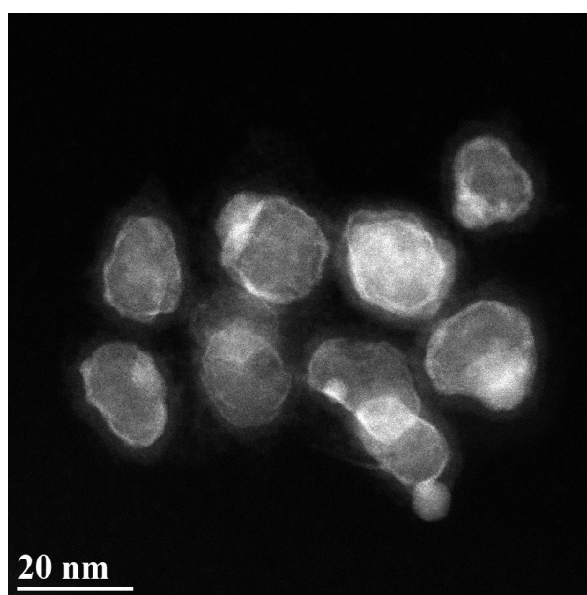
Figure S3. HAADF image of the original NiAu after oxidation at 350 $^{\circ}$C in air.
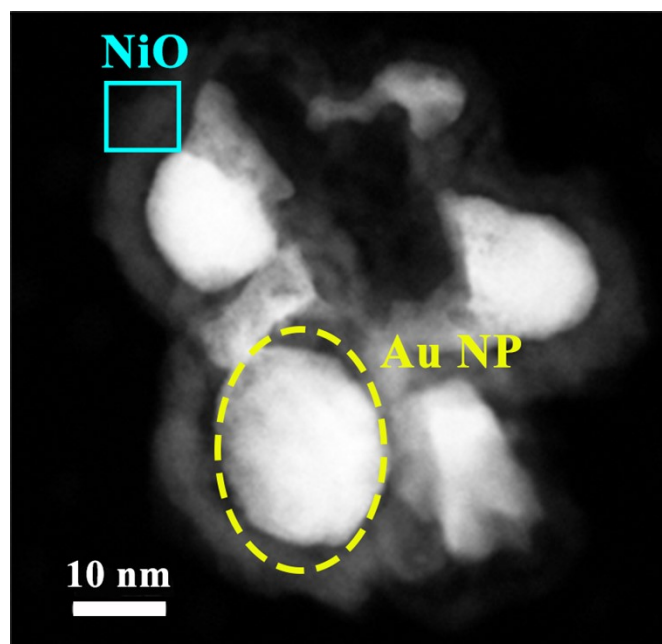
**Figure S4.** HAADF images of original NiAu after rapid oxidation at 300 ^{o}C for 5 min in the air.

Figure S5. HAADF images of original NiAu after being calcined at 600 ^{o}C for 1 h in the air. a) Low magnification; b) High magnification.

Note in Fig. S5. The bright dots are the Au clusters on the NiO matrix surface, and some Au species cannot be clearly imaged, suggesting that it's not on the outmost

surface, but embedded by a depth below the matrix surface. The above dispersion status of Au species further accounts the circle-like pattern marked in Fig. S5a, where small Au clusters are embedded in NiO matrix at a uniform depth.
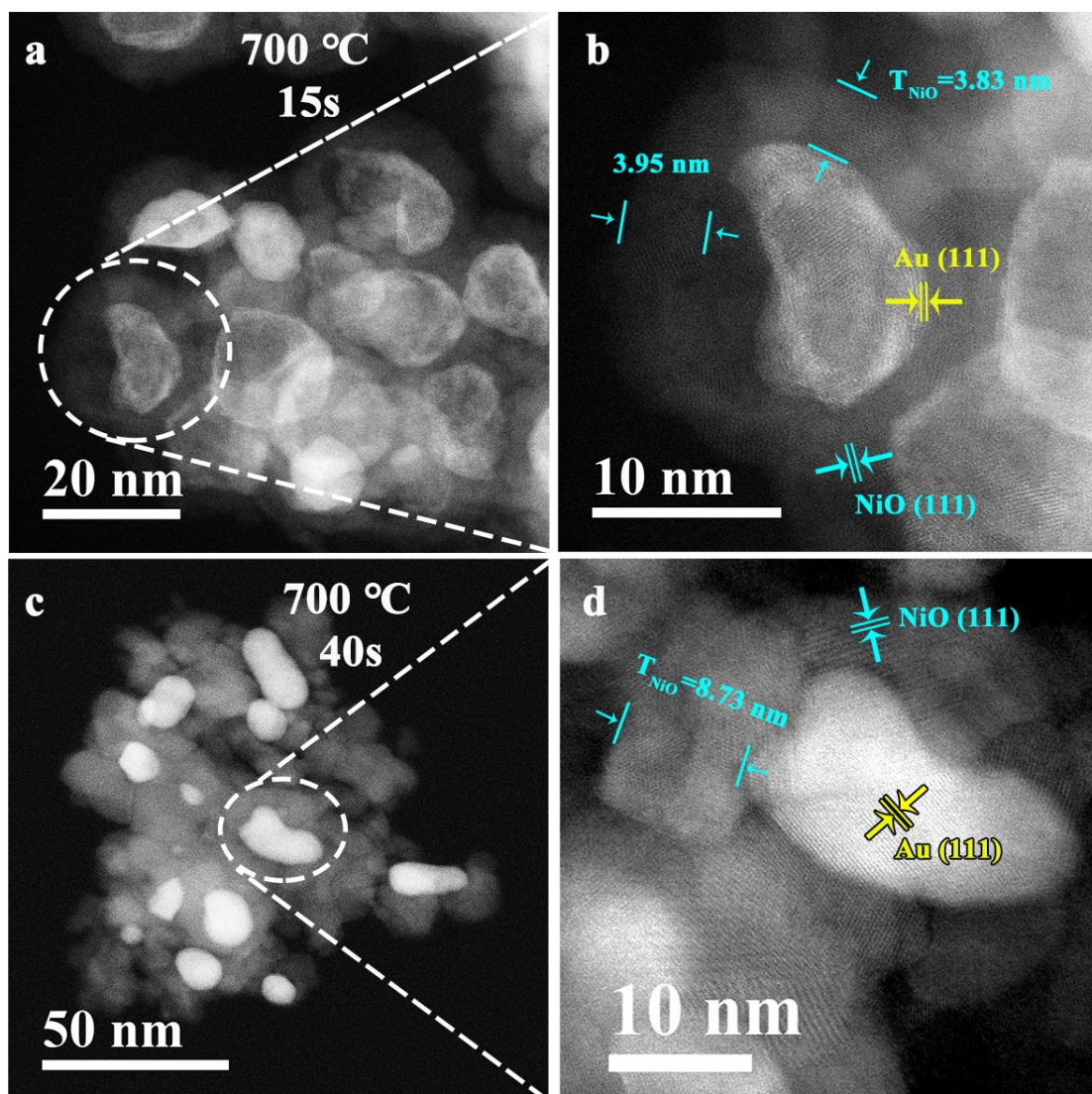

Figure S6. NiAu nanostructure after flash burning at 700 °C. a, c) original NiAu treated at 700 °C for 15s and 40s, respectively. b, d) enlarged view of the red circled area in a and c, respectively.

Note on Fig. S6. Flash burning is an efficient method relying on a fast high

temperature thermal treatment, and it has been commonly used for removing the organic ligands and studying a variety of structure–activity relationships.[7] As shown in Fig. S6, the diffusion tendencies of Ni and Au atoms at 700 °C oxidative treatment are similar as the sample going through a slow oxidative annealing in oven. For 15s, NiO shell grows into a thickness of nearly 4nm, Au disperses inside the shell and shrinks into particle separated from the NiO shell. The Ni@Au@NiO multilayered nanostructure has similar configuration with the sample endures slowly oxidation at 350 °C. The structure reconstruction obviously occurred in such short time, indicating flash burning is not inappropriate for removing the residual organic precursor of fresh NiAu. For 40s, NiO and Au components separate totally from each other. Au sinters into bulk spheres. The thickness of NiO layers is larger than 8.7 nm and presents a serious sintering status, which is similar with the sample calcinated at 600 °C in air.

200 nm
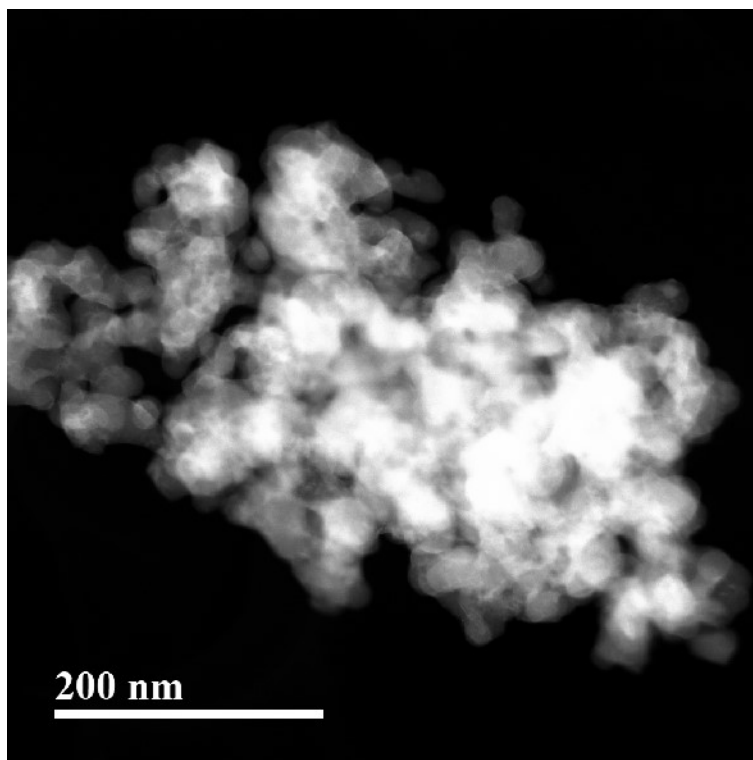
Figure S7. HAADF images of NiAu NDBs after hydrogen TGA (Thermo Gravimetric Analyzer).
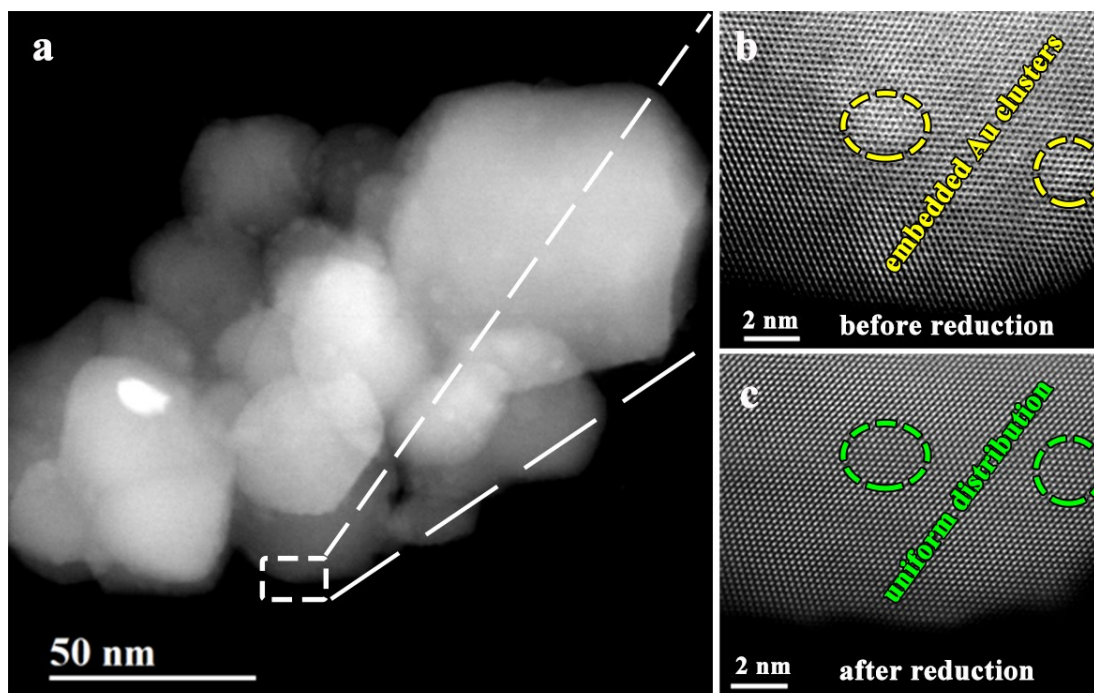
Figure S8. HAADF images of the sample (original NiAu calcinated at 600 °C in air before and after reduction. a-b) the sample before reduction and b is the enlarged view of red rectangle in a; c) enlarged view of red rectangle in a after the reduction.
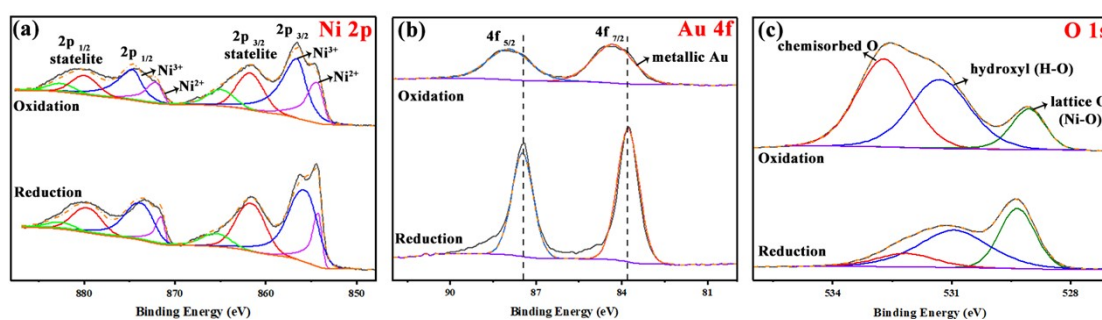
Figure S9. High-resolution XPS spectra of Ni 2p (a), Au 4f (b) and O 1s (c) for Oxi- and Red-NiAu, respectively.

Note on Fig. S9. The surface compositions and valence states of the original NiAu after oxidation at 350 °C (Oxi-NiAu) and reduction at 250 °C (Red-NiAu) are investigated by X-ray photoelectron spectroscopy (XPS). The high-resolution spectra of Ni 2p, Au 4f and O1s are displayed in Fig. S9. There are two main peaks (Ni 2p$_{3/2}$

and Ni $2p_{1/2}$) and two corresponding satellite peaks for Ni 2p orbit (Fig. S9a). According to the pervious literatures, the multiple-split of Ni $2p_{3/2}$ suggests the formation of the NiO layer which is composed of Ni^{2+} (NiO) and Ni^{3+} (Ni_2O_3), and $Ni^{(III)}_2O_3$ commonly forms and co-exist with $Ni^{(II)}O$ during Ni oxidation.[8] Noting that, the spectrum of Ni 2p for Red-NiAu also indicates the existence of the NiO layer, and the obvious peak of lattice O in O 1s spectra confirms the existence of NiO layer as well. This can be mainly because of the easy oxidation of Ni under air exposure based on previous studies.[1] Since XPS can only probe the chemical information of a few atomic layers near the surface, the states of Ni in Ni core for both Oxi-NiAu and Red-NiAu is hardly detected, which may explain the lack of metallic Ni signal.[9] Meanwhile, the Au in both Oxi-NiAu and Red-NiAu are mainly metallic, indicating the well reduction of Au during synthesis. The BE of Au $4f_{7/2}$ for Oxi-NiAu is 84.3 eV (slightly higher than that of 84 eV for pure Au reported by previous work), which is probably due to the electron transfer from Au to NiO layer.[10] It is noteworthy that BE of Au $4f_{7/2}$ for Red-NiAu (about 83.8 eV) exhibits an obvious shift toward lower BE compared with Oxi-NiAu, which indicates the different Au species in Red-NiAu (Fig. S9b). Combining with the current TEM data and previous works, the shift can be mainly attributed to the formation of NiAu alloy, and the electron transfers from Ni to Au due to the higher electronegativity of Au (2.54 for Au and 1.91 for Ni).[11] In addition, the O 1s spectra show the obviously decreased ratio of chemisorbed O after reduction (Fig. S9c), which can be probably owing to the lower adsorption capacity of O for compact NiO layer which is formed during the oxidation at room temperature (based on our pervious study[1,12]) compared with the fractured one formed in promoted oxidation at 350 °C (Fig. 2g).
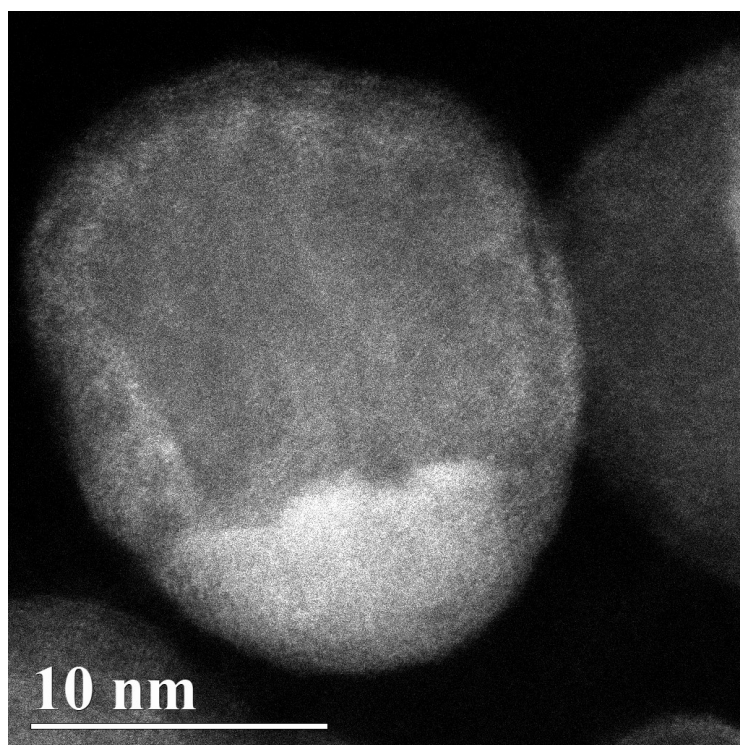
Figure S10. HAADF image of the oxidized NiAu (calcined at 350 °C in air) after reduction.

Note on Fig. S10. It can be seen that although Au atoms remain a shell-like dispersion which is the same as the dispersion of Au atoms in oxidated sample, they have migrated to a certain depth on the surface to form the NiAu alloy phase. This depicts the same tendency as the original NiAu during reduction.
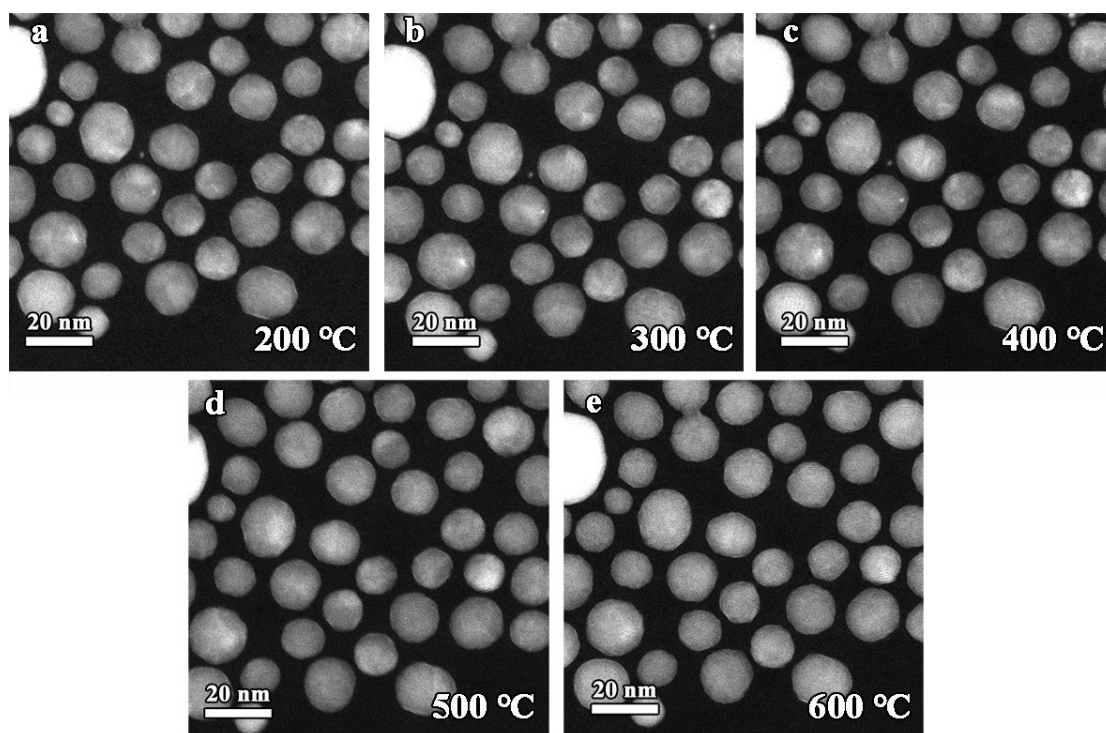
Figure S11. In situ observation of the original NiAu during reductive treatment at different temperatures. 200 ^{o}C (a), 300 ^{o}C (b), 400 ^{o}C (c), 500 ^{o}C (d) and 600 ^{o}C (e), respectively. The pressure is 1.3×10^{-2} Pa.
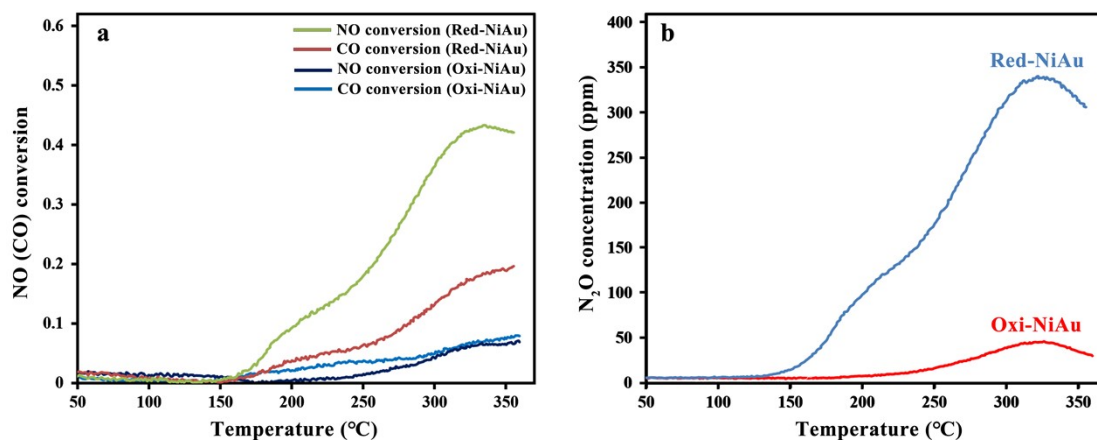
Figure S12. The catalytic performance of the Red-NiAu and Oxi-NiAu catalyst for CO-NO reaction. a) NO and CO conversion during the catalytic procedure. b) the concentration of N_2O during the catalytic procedure.

Note on Fig. S12. As displayed in Fig. S12a, the conversion rate of either NO or CO

reaches to only ~10% at 350 °C for the Oxi-NiAu catalyst although more Au sites are formed owned to the transfer from Au tip (bulk particle in nanometers) to few well dispersed atom-layered Au shell. Compared with Oxi-NiAu, Red-NiAu exhibits much higher catalytic activity, where NO conversion rate rises up to over 40% and ratio of CO: NO changes to about 1:2. It is noteworthy that except promoted conversion rate, the Red-NiAu also lower the light-off temperature from ~220 °C to 150 °C. In addition, NO conversion slightly decreases while the CO conversion continuous increase for Red-NiAu after ~325 °C suggesting higher averaged oxidizing status of N_xO species. Combining with the trend of N_2O concentration that achieved maximum at about 325 °C and then descended with the raising temperature for both Oxi- and Red-NiAu (Fig. S12b), it can be deduced that higher N_2 selectivity has to exist to fully oxidize CO substance.[13]
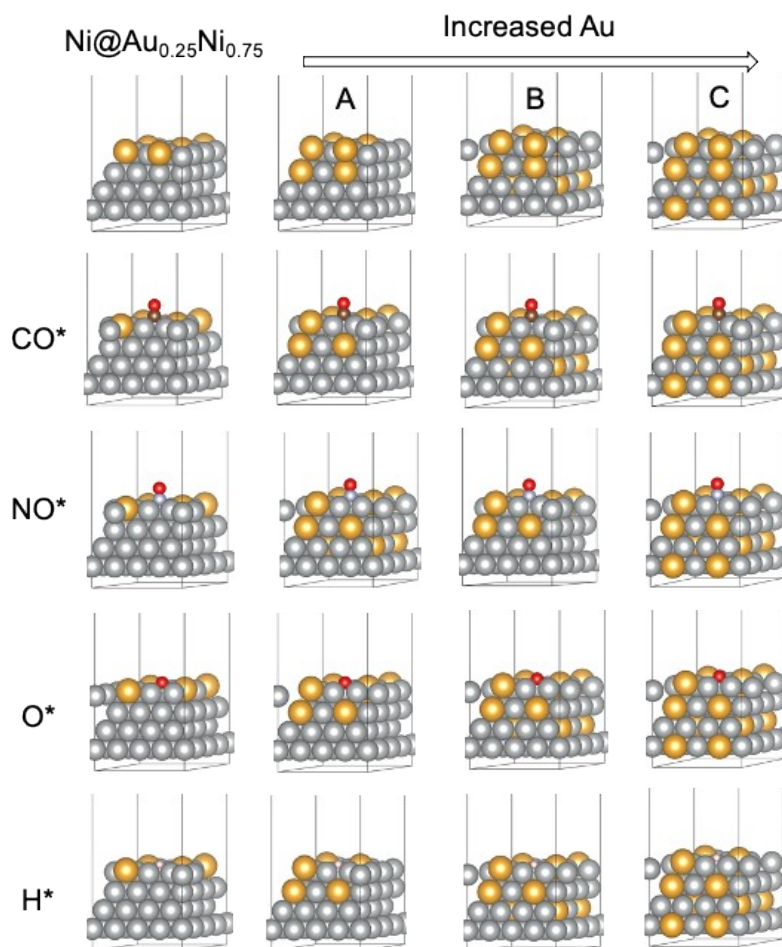
Figure S13. Optimized structures of the adsorption configurations with increased Au composition in the sublayers.

References

1. W. Liu, K. Sun, R. Wang, In situ atom-resolved tracing of element diffusion in NiAu nanospindles. *Nanoscale*, 2013, **5**, 5067-5072.

2. J. P. Perdew, K. Burke, M. Ernzerhof, Generalized gradient approximation made simple. *Phys. Rev. Lett.*, 1996, **77**, 3865–3868.

3. W. Kohn, L. J. Sham, Self-consistent equations including exchange and correlation effects. *Phys. Rev.*, 1965, **140**, A1133.

4. H. Monkhorst, J. Pack, Special points for brillouin zone integrations. *Phys. Rev. B*, 1976, **13**, 5188–5192.

5. A. H. Larsen, J. J. Mortensen, J. Blomqvist, I. E. Castelli, R. Christensen, M. Dułak, J. Friis, M. N. Groves, B. Hammer, C. Hargus, et al. The atomic simulation environment - A Python library for working with atoms. *J. Phys. Condens. Matter.*, 2017, **29**, 273002.

6. H. Li, K. Shin, G. Henkelman, Effects of ensembles, ligand, and strain on adsorbate binding to alloy surfaces. *J Chem. Phys.*, 2018, **149**, 174705.

7. M. Cargnello, C. Chen, B. T. Diroll, V. V. Doan-Nguyen, R. J. Gorte, C. B. Murray, Efficient removal of organic ligands from supported nanocrystals by fast thermal annealing enables catalytic studies on well-defined active phases. *J. Am. Chem. Soc.*, 2015, **137**, 6906-6911.

8. Z. Qiu, H. Gong, G. Zheng, S. Yuan, H. Zhang, X. Zhu, H. Zhou, B. Cao, Enhanced physical properties of pulsed laser deposited NiO films via annealing and lithium doping for improving perovskite solar cell efficiency. *J. Mater. Chem. C*, 2017, **5**, 7084-7094.

9. X. Yan, L. Tian, X. Chen, Crystalline/amorphous Ni/NiO core/shell nanosheets as highly active electrocatalysts for hydrogen evolution reaction. *J. Power Sources*, 2015, **300**, 336-343.

10. Q. Fang, Z. Qin, Y. Shi, F. Liu, S. Barkaoui, H. Abroshan, G. Li, Au/NiO composite: A catalyst for one-pot cascade conversion of furfural. *ACS Appl. Energy Mater.*, 2019, **2**, 2654-2661.

11. C. Cai, S. Han, W. Liu, K. Sun, L. Qiao, S. Li, X. Zu, Tuning catalytic performance by controlling reconstruction process in operando condition. *Appl. Catal., B*, 2020, **260**, 118103.

12. X. Xiang, J. Nie, K. Sun, L. Zhang, W. Liu, J. Schwank, S. Wang, M. Zhong, F. Gao, X. Zu, Structure evolution of NiAu nanoparticles under ambient conditions revealed directly by atom-resolved imaging combined with DFT simulation. *Nanoscale*, 2014, **6**, 12898-12904.

13. Z. Xu, Y. Li, Y. Lin, T. Zhu, A review of the catalysts used in the reduction of NO by CO for gas purification. *Environ. Sci. Pollut. Res.*, 2020, **27**, 6723-6748.